PNAS RESEARCH ARTICLE | EARTH, ATMOSPHERIC, AND PLANETARY SCIENCES OPEN ACCESS

Rapid seafloor changes associated with the degradation of Arctic submarine permafrost

Charles K. Paull[a,1,2], Scott R. Dallimore[b,2], Young Keun Jin[c], David W. Caress[a], Eve Lundsten[a], Roberto Gwiazda[a], Krystle Anderson[a], John Hughes Clarke[d], Scott Youngblut[e], and Humfrey Melling[f]

Edited by Michael Manga, University of California, Berkeley, CA; received October 22, 2021; accepted February 2, 2022

Repeated high-resolution bathymetric surveys of the shelf edge of the Canadian Beaufort Sea during 2- to 9-y-long survey intervals reveal rapid morphological changes. New steep-sided depressions up to 28 m in depth developed, and lateral retreat along scarp faces occurred at multiple sites. These morphological changes appeared between 120-m and 150-m water depth, near the maximum limit of the submerged glacial-age permafrost, and are attributed to permafrost thawing where ascending groundwater is concentrated along the relict permafrost boundary. The groundwater is produced by the regional thawing of the permafrost base due to the shift in the geothermal gradient as a result of the interglacial transgression of the shelf. In contrast, where groundwater discharge is reduced, sediments freeze at the ambient sea bottom temperature of ∼−1.4 °C. The consequent expansion of freezing sediment creates ice-cored topographic highs or pingos, which are particularly abundant adjacent to the discharge area.

permafrost | Arctic | repeat mapping | pingos | thermokarst

Significance

Temperature increases in Arctic regions have focused attention on permafrost degradation on land, whereas little is known about the dynamics of extensive glacial-age permafrost bodies now submerged under the vast Arctic Continental shelves. Repeated high-resolution bathymetric surveys show that extraordinarily rapid morphologic changes are occurring at the edge of the continental slope of the Canadian Beaufort Sea along what was once the seaward limit of relict Pleistocene permafrost. How widespread similar changes are on the Arctic shelves is unknown, as this is one of the first areas in the Arctic subjected to multiple multibeam bathymetric surveys. Rapid morphologic changes associated with active submarine permafrost thawing may be an important process in sculpturing the seafloor in other submarine permafrost settings.

The effects of on-going terrestrial permafrost degradation (1–3) have been appraised by comparison of sequential images of Arctic landscapes that show geomorphic changes attributed primarily to thermokarst activity induced by recent atmospheric warming and ongoing natural periglacial processes (4–8). While the existence of extensive relict submarine permafrost on the continental shelves in the Arctic has been known for years (9, 10), the dynamics of submarine permafrost growth and decay and consequent modifications of seafloor morphology are largely unexplored.

Throughout the Pleistocene, much of the vast continental shelf areas of the Arctic Ocean experienced marine transgressions and regressions associated with ∼125-m global sea level changes (11). Extensive terrestrial permafrost formed during sea-level low stands when the mean annual air temperatures of the exposed shelves were less than −15 °C (11, 12). Exploration wells drilled on the continental shelf in the Canadian Beaufort Sea show that relict terrestrial permafrost occurs in places to depths >600 m below seafloor (mbsf) and forms a seaward-thinning wedge beneath the outer shelf (10, 13, 14) (Fig. 1 *A* and *B*). The hydrography of the Canadian Beaufort Sea slows the degradation of the relict permafrost because a cold-water layer with temperatures usually near -1.4 °C blankets the seafloor from midshelf depths down to ∼200-m water depth (mwd) (15, 16) (Fig. 1*B*). As the freezing point temperature of interstitial waters is also controlled by salinity and sediment grain size, partially frozen sediments occur in a zone delimited by the ∼−2 °C and 0 °C isotherms (17, 18) (Fig. 1*B*).

Distinctive surface morphologies characterize terrestrial permafrost areas. Conical hills (3 to 100 m in diameter) called pingos are common in the Arctic (19, 20). Pingos are formed due to freezing of groundwater. They characteristically contain lenses of nearly pure ground ice that cause heaving of the ground surface. Positive relief features with similar dimensions, referred to as pingo-like features (PLFs), are scattered across the Canadian Beaufort shelf (21, 22). On land, permafrost thawing, where there is ground ice in excess of the sediment pore space, can induce sediment consolidation (23), and surface subsidence results in widespread thermokarst landforms. Among the more dramatic occurrences are retrogressive thaw slumps (4–8, 24). These form where ice-rich permafrost experiences surface thaw causing thaw settlement and release of liquified sediment flows. Because of the loss of volume associated with thawing of massive ground ice, thaw slumps can quickly denude permafrost landscapes.

During the first systematic multibeam mapping surveys in 2010 covering part of the shelf edge and slope in the Canadian Beaufort Sea, a band of unusually rough seafloor morphology between ∼120 and ∼200 mwds (25) was discovered along a ∼95-km-long stretch of the shelf. Subsequently, three additional multibeam surveys covering small characteristic areas (Fig. 2*A*) were conducted to understand the processes responsible for the observed morphologies. Here, we document the unique morphologies and

Author contributions: C.K.P., S.R.D., Y.K.J., J.H.C., and H.M. designed research; C.K.P., S.R.D., Y.K.J., E.L., R.G., K.A., J.H.C., S.Y., and H.M. performed research; D.W.C. contributed new reagents/analytic tools; C.K.P., S.R.D., D.W.C., E.L., R.G., K.A., and H.M. analyzed data; and C.K.P., S.R.D., and R.G. wrote the paper.

The authors declare no competing interest.

This article is a PNAS Direct Submission.

[1]To whom correspondence may be addressed. Email: paull@mbari.org.

[2]C.K.P. and S.R.D. contributed equally to this work.

Published March 14, 2022.

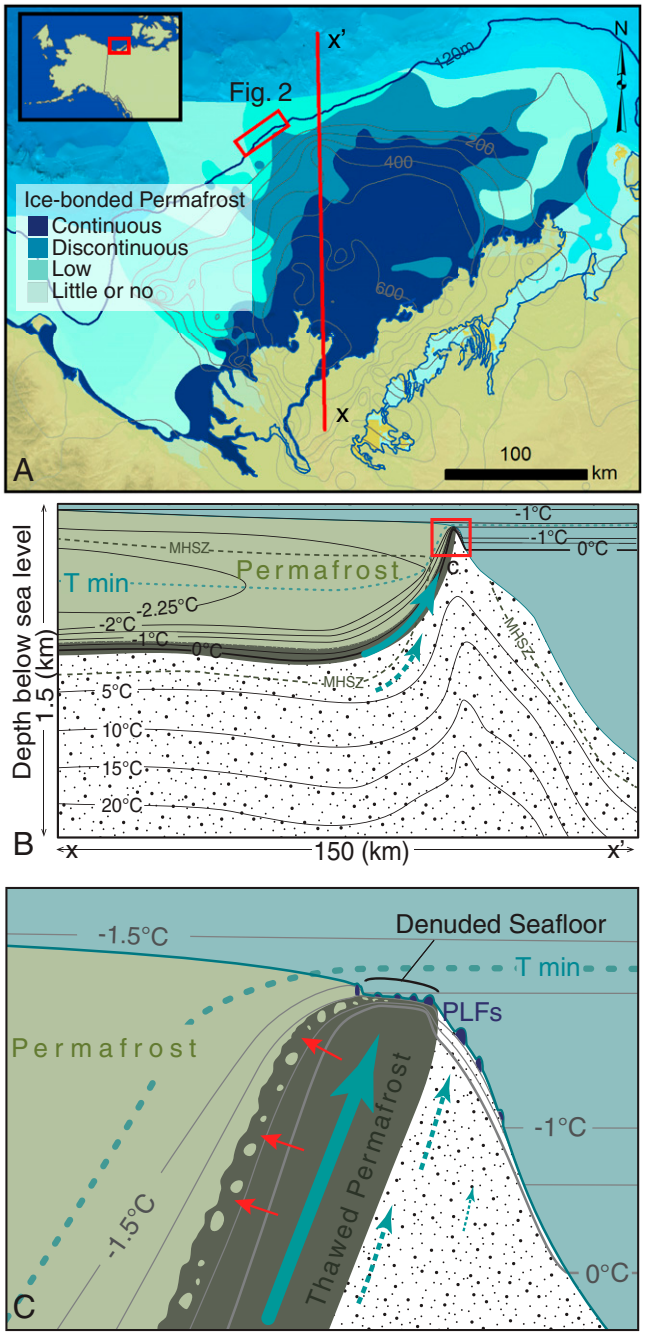

Fig. 1. Map and cross-section showing the relationship between shelf edge morphology and the subsurface thermal structure along the shelf edge in the Canadian Beaufort Sea. (*A*) Shows the location of the study area with respect to estimates of submarine permafrost density (see key) and thickness, modified after 14. Thin contours indicate permafrost thickness in meters. Thicker contour is 120-m isobath marking the shelf edge. Area of repeat mapping coverage shown in Fig. 2 is indicated with a red box. (*B*) Shows a schematic cross-section with contours of selected subsurface isotherms modified after 15 along line x-x' in *A*. The dotted blue line illustrates a thermal minimum (T-min) running through the relict permafrost isotherm and Beaufort Sea waters (16). Green shading indicates relict permafrost. Turquoise arrows show inferred flow of water from permafrost thawing along the base of the relict permafrost to the seafloor. The brown area indicates the zone where relict Pleistocene permafrost is predicted to have thawed with consequent movement of liberated groundwater, associated latent heat transfer and thaw consolidation causing surface settlement. Dashed brown lines define the subbottom limits for methane hydrate stability zone (MHSZ) which starts at ~240 m below the sea surface and extends into the subsurface depending on the pressure and temperature gradient. The red box indicates the area shown in more detail in *C* with the same color scheme. The area of denuded seafloor in *C* is flanked by PLFs (dark-blue fill). Red arrows indicate the direction of heat transfer along the seaward edge of relict permafrost wedge.

seafloor change in this area and explore how the seafloor features may be related to subsea permafrost degradation and formation.

Results

Rapid Changes in Seafloor Morphology. Differences measured in four multibeam bathymetric surveys over a 9-y period (2010 to 2019) covering the same area yielded three snapshots of changes in seafloor morphology. Areas where the seafloor deepened between surveys experienced a volume loss and were observed as being roughly circular or oval-shaped polygons (Figs. 2*B*, 3, and 4 *A* and *B*). Volume losses occurred on steep slopes found on the flanks of preexisting scarps or within closed depressions, as well as on the crests of local ridges. The volume losses characteristically left irregularly shaped steep-sided depressions (Figs. 2*A*, 3, 4*A*, and 5*A*).

The largest repeat mapping area covered a 25.9-km^2 area (~10-km long and ~2.5-km wide section of the shelf edge and uppermost slope), surveyed in 2010 and 2019 using ship-mounted multibeam sonars (Fig. 2*A*). Differences between these grids showed 41 sites where the maximum seafloor deepening was large enough to be resolved with a high degree of confidence (e.g., averaging 6.7 m) during the 9-y period within the area covered by both surface ship multibeam surveys (Fig. 2*A*). The side slopes of the newly developed depressions typically exceeded 60°. The greatest change was the formation of an oval-shaped depression up to 29 m deep, 225 m long, and 95 m wide (Fig. 3). This new depression (net volume loss of ~2.9 × 10^5 m^3) developed where a ~200-m-long linear ridge had previously existed.

Surveys conducted in 2013 and 2017 with an autonomous underwater vehicle (AUV) collected higher resolution bathymetry (0.87-m resolution vs. 4-m and 2-m resolution from surface ship multibeam in 2010 and 2019, respectively), allowing the changes in seafloor morphology to be tracked over three time intervals (2010 to 2013, 2013 to 2017, and 2017 to 2019). Within the 4.8-km^2 area common to all four surveys (Fig. 2*B*), nine sites of changes were identified in this 9-y time period. Changes were detected at seven sites during just one of the three time intervals. One depression developed on the crest of a ridge and enlarged during each of the subsequent survey intervals. Two neighboring sites also successively expanded but only during two of the survey intervals, with one being along a scarp and another developing a new depression on the flank of a ridge.

Local areas of positive seafloor change also occurred. The gains typically occurred in previous lows and downslope of areas that experienced a volume loss. However, these gains averaged less than 5% of the volume losses in the adjacent ridges. Only one site covered in the 2010 to 2019 surveys showed an overall positive change (i.e., local volume increase). It was at the bottom of a depression that created a flat-topped infilled sediment pond. Altogether, areas of volume gain did not accommodate the observed volume losses. The new depressions represented a net volume loss of 6.1 × 10^5 m^3 from an area with detectable seafloor change totaling 1.7 × 10^5 m^2.

The study area was situated at the transition between the outer continental shelf and upper slope and was characterized by distinctive morphologic bands (Fig. 2*C*). A distinct break in slope in 125 to 135 mwd, frequently associated with a regional scarp, marked the seaward edge of the outer continental shelf. Above the scarp, the seafloor surface was generally continuous with a smooth regional surface that slopes seaward at <0.8°,

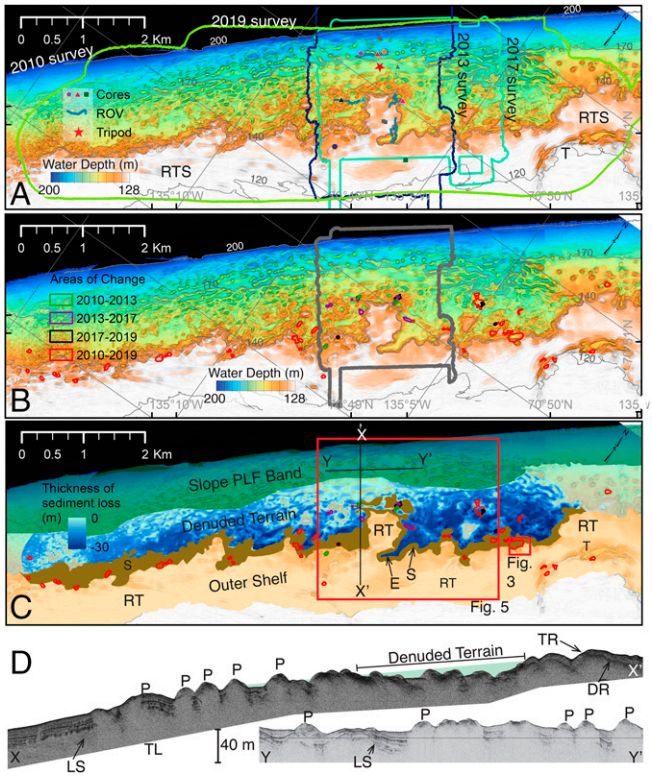

Fig. 2. (*A*) Shows bathymetry of a small section of the shelf edge indicated in Fig. 1*A*, with a color scale going from white (128 m) to blue (200 m) and contours at 120, 140, 170, and 200 mbsf. Outlines of areas resurveyed in 2013 (blue), 2017 (turquoise), and 2019 (green) are superimposed on the 2019 and regional 2010 survey. Colored symbols indicate locations of cores with porewater data using same key as Fig. 5*B*. The red star indicates the location of a temperature tripod deployed in the period 2015 to 2016. The location of ROV dive tracks (blue paths) are indicated. (*B*) Covers the same area as *A* with polygons identifying sites where changes were noted between surveys as follows: 2010 to 2013 (green), 2013 to 2017 (purple), 2017 to 2019 (black), and 2010 and 2019 (red). (*C*) Shows the same area, colored according to the difference in bathymetry between the 2019 survey and an idealized smooth surface extending between the top of the shelf edge scarp and the layered sediments occurring between the numerous PLFs. This is used to estimate the volume of material that eroded assuming the earlier Holocene seafloor corresponded with this idealized surface. Three zones of topography are labeled. Red boxes are locations of Figs. 3 and 5. (*D*) Shows Chirp profiles with the position of profiles shown in *C* and Fig. 5*A*. Light-green backdrop in X-X′ indicates possible void produced by retrogressive slide retreat used to calculated volume loss. Also indicated are TL, tilted layers; P, pingo-like-feature; and DR, diffuse reflector.

characteristic of the outer shelf (25) (regional terrace [RT], Figs. 2 and 5*A*). Within ∼1 km of the scarp, this regional surface showed gentle undulations (Fig. 5*A*), as well as a few steep-sided circular to oval-shaped depressions, a kilometer-long linear trough, and scattered PLFs (Figs. 2*C* and 4 *D* and *E*). During the 2010 to 2019 time interval, six sites of change were recorded on the outer shelf landward of the main scarp associated with depressions and troughs (trough [T], Fig. 2*C*). Twenty-eight sites with volume loss (2010 to 2019) were found along the face of the regional scarp suggesting retrogression of the scarp into the shelf. The morphology of the scarp consisted of multiple arcuate indentations similar to scars observed at sites where the difference grids showed volume losses (locations of scarp [S], Figs. 2, 4*A*, and 5*A*). The largest indentation consisted of a >500-m-long and >100-m-wide embayment that nearly isolated a distinct headland in the regional terrace (embayment [E] and RT, Figs. 2*A* and 5*A*). Remotely operated vehicle (ROV) observations showed the flanks of the embayment consisted of angular near-vertical faces of competent mud, developed along joints (Fig. 5*A*), and Chirp profiles showed roughly seafloor-parallel reflectors which truncate along the scarp face (truncated reflector [TR], Fig. 2*D*).

Below the regional scarp in ∼140 to ∼170 mwd was a ∼1-km-wide zone of especially rough denuded terrain composed of multiple closed, circular- to ovoid-shaped depressions up to 16 m deep and erratically oriented ridges (Figs. 2*C*, 4 *A* and *B*, and 5*A*). Seven sites of measured volume loss (2010 to 2019) occurred within this denuded zone away from the scarp (Fig. 2*C*). These changes occurred where topographic highs, ridge crests, or the sides of steep slopes had collapsed, often enlarging and deepening existing depressions. No resolvable internal structures were seen in Chirp subbottom profiles from this zone (Fig. 2*D*).

The band of seafloor between ∼170 and ∼200 mwd was characterized by numerous circular topographic highs or PLFs, identified as the slope PLF band (Fig. 2*C*). They were typically 50 m in diameter, standing up to 10 m above the surrounding seafloor (Figs. 2, 4*C*, and 5*A*). Often, PLFs occurred on isobath-parallel ridges. No changes were observed in this band or at greater water depths by the repeat surveys. Chirp profiles showed continuous reflector packages of variable dips in the troughs between the PLF and ridges, suggesting the physical continuity of the strata are disrupted, but not incised by erosion (Fig. 2*D*). Similar marine sediments of postglacial and Holocene age are known to cover the continental slope regionally (25–27). The 1-m grid resolution AUV bathymetry (2013 and 2017) showed most PLFs have depressions on their crest of varying sizes and depths (Fig. 4 *D* and *E*). However, a continuous smooth surface consistently covers the area between these PLFs, usually their flanks and even the crests of some PLFs (Fig. 4 *C*–*E*). ROV observations showed the central depressions of PLFs have inner walls with angular jointed faces.

Below 200 mwd, the seafloor was generally smooth and dipped at the ∼2.5° angle, characteristic of the regional continental slope. Chirp profiles showed that the upper ∼30 m of the slope contained laterally continuous and closely spaced reflectors that were nearly parallel to the present seafloor but thin toward the shelf edge (layered sediment [LS], Fig. 2*D*).

Porewater chloride concentrations in sediment cores taken from the outer shelf to the slope PLF band showed freshening at depth. A downward linear extrapolation of the measured gradients indicated that waters with <400 mM chloride commonly occurred at <20-m subbottom depths within this area (Fig. 5*B*). Cores from PLFs within the study area and nearby have sampled pore and lens ice (28, 29). ROV surveys and sediment coring have not found evidence of significant methane seepage within this study area (27, 28).

Discussion

Considerable net volume losses were documented within the denuded zone to account for the lateral scarp retreat and the enlargement of closed depressions and troughs observed during the 9-y-long repeat mapping period (Fig. 2 *B* and *C*). The seafloor morphology remained similar between the areas of the observed changes (Fig. 4 *A* and *B*) and the widespread morphologies within the denuded zone (Figs. 2 and 4*F*). This suggests that this seascape is the cumulative result of morphology-changing processes acting at small spatial scales but operating throughout the denuded zone over longer time periods. To constrain the net volume loss inferred within the denuded zone, a surface was fitted that extends across the zone of rough eroded terrain from the regional terrace surface on top of the scarp to the top of the

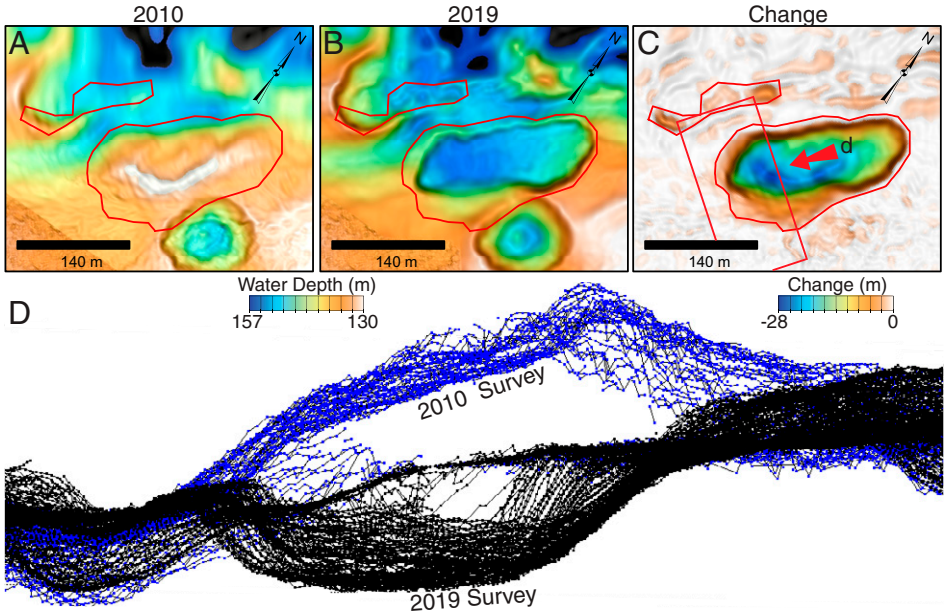

Fig. 3. Images showing the largest observed seafloor change between the 2010 and 2019 multibeam surveys. Location of this depression in the regional map is shown in Fig. 2*C*. (*A* and *B*) Show the bathymetries measured in 2010 and 2019, respectively. (*C*) Shows the difference between these grids with a color scale going from 0 to −28 m. (*A*, *B*, and *C*) Cover the same area with polygon of change outlined in a thin red line. (*D*) A perspective view of the multibeam sounding data used to generate bathymetric grids in the area indicated by the red box in *C* with 2010 in blue and 2019 in black. Red arrow in *C* is the direction of the perspective view.

stratified postglacial marine sediments found between the PLFs below 170 m (RT and LS, Fig. 2 *C* and *D*). The space between this idealized former seafloor surface and the present-day seafloor represents a volume loss of ∼7.5 × 10^7 m^3, averaging 9 m throughout the denuded zone. At a volume loss rate of 6.5 × 10^4 m^3 per year within the denuded zone alone, as measured over the 2010 to 2019 time period, ∼1,150 y would have been required to generate this topography.

Formation of Enclosed Depressions and Retreating Scarps with Net Lost Volume. The rapid formation of isolated circular holes within permafrost areas in the Siberian tundra has been attributed to spontaneous methane eruptions (24, 30). Given that the viscosity of water is 55 times higher than that of air, ejecta excavated by seafloor eruptions would not travel far. However, ejecta rims or other debris at the scale required to account for the missing volume in the denuded zone, or even the net volume loss observed over the last 9 y, were absent. The possibility of an eruptive origin for the observed depressions would require the existence of impermeable seals over gas-filled voids. However, the presence of brackish waters within the shelf edge and adjacent slope sediments indicated widespread groundwater flow, which is inconsistent with a sealed system where overpressure would develop. The continued enlargement of some depressions observed over multiple surveys indicates that the development of these depressions is part of on-going processes. The rapid recharge of subsurface gas pockets followed by repeated spontaneous eruptions is hard to envision. Thus, other mechanisms which account for the missing volume are considered.

We propose the lateral scarp retreat and the formation of enclosed depressions observed here (Figs. 3 and 4*F*) result from surface material subsiding or collapsing into fluid filled voids that had been previously occupied by a solid phase. In principle, either methane hydrate or permafrost ice could have been part of the solid phase supporting the overburden. Whereas methane hydrate does occur in places within and below relict permafrost (15, 22, 31), massive subsurface methane hydrate deposits have not been sampled in this region, and gas hydrate deposits occupying large fractions of the sediment volume are uncommon anywhere (31). Moreover, there is little indication that the leaking waters contain significant concentrations of methane (27).

Relict permafrost likely once existed beneath the denuded terrain (10, 12, 14, 32) (Fig. 1*A*). The denuded zone lies at or near the probable contact between the former permafrost-bearing sediments and strata that were entirely marine during the last glacial period when global sea level was ∼125 m lower than present (11). As the Beaufort Shelf did not support a thick ice cap, it experienced only minor postglacial isostatic adjustment (33–35). Thus, the outer shelf (i.e., ∼≤125 mwd) was exposed to cold subaerial conditions during Pleistocene low stands, which is appropriate to develop permafrost (Fig. 1*B*). Evidence of widespread permafrost on the outer shelf is supported by well logs from exploratory drilling (36), which indicate ice can exceed more than 30% of the sediment volume (37, 38), and by the high seismic velocities within subsurface sediments inferred from seismic refraction studies (14, 39). However, seismic velocities near the shelf edge are indicative of only partial or absent ice bonding (Fig. 1*A*). We attribute the denuded terrain (Fig. 2*C*) to sea floor settlement due to subsurface volume loss as a result of relict permafrost degradation.

Degradation of terrestrial Arctic permafrost is commonly attributed to mean annual temperature increases (4–8). The water temperature measurements made during ROV dives, on hydrocasts, and from moorings show the area where the denuded seafloor occurs is usually bathed in waters that are ∼−1.4 °C (16, 17). However, the denuded zone depth range is near a sharp halocline, typically at >200 mwd, which separates the warmer-deeper-saltier Atlantic waters from the colder-shallower-fresher Pacific waters that cap the western Arctic Ocean. Occasionally, the position of this thermocline shoals, exposing the seafloor to warmer conditions. A bottom temperature lander deployed for 1 y on a tripod 1.6 m above the seafloor in

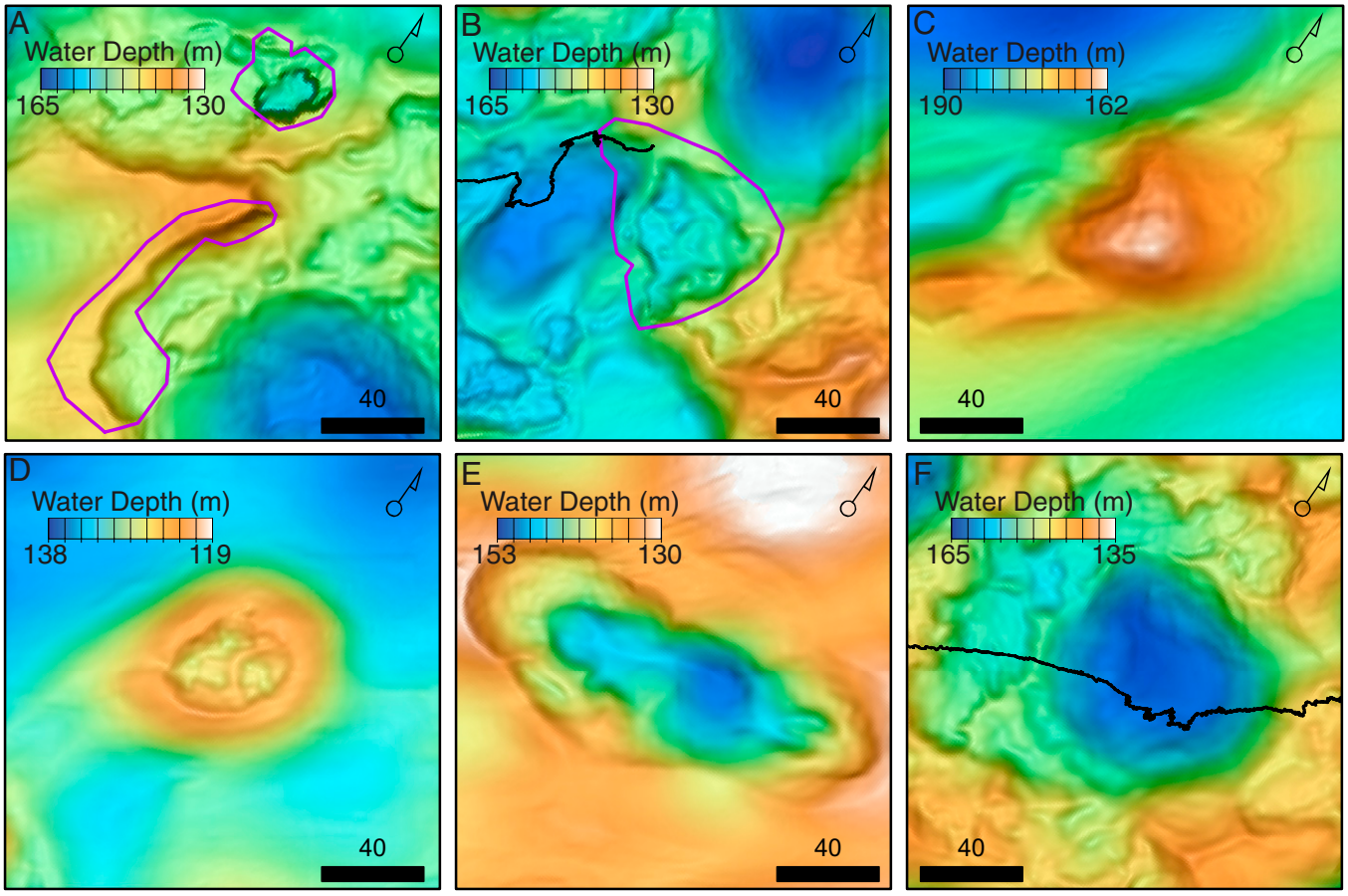

Fig. 4. Selected areas of 1-m resolution bathymetry collected by the AUV in 2017 showing seafloor morphology. Locations of *A* to *F* are indicated in Fig. 5*A*. *A* and *B* have polygons showing where differences between AUV surveys (2013 to 2017) detected significant volume losses. *C*–*F* show different areas representing a progression from a nearly smooth-surfaced PLF (*A*) to those with increasingly large depressions (*D*–*F*). Black lines in *B* and *F* show the approximate ROV path on the bottom.

2015 to 2016 at 165 mwd within the repeat mapping area (Fig. 2*A*) recorded a 2.1 °C range in bottom water temperatures with month-long warm excursion reaching 0.5 °C before dropping back to −1.5 °C (40). The propagation of such short-term bottom water temperature excursions into the sediments is very shallow as this transient effect is dampened within a few meters subsurface. It is therefore unlikely that such temperature excursions are the primary cause for subsurface permafrost degradation (41). For thermal effects to impact permafrost at greater depths requires changes in the mean annual bottom water temperature. Although observations are limited, the existence of systematic unidirectional changes in the mean annual temperature of bottom waters during the late Holocene in this region is not known (17, 42).

A profound shift in the sediment mean annual temperature took place when the shelf was transgressed at the end of the last glaciation at ∼12,000 y ago (10–12, 15, 18). Transgression reversed the temperature gradient in the upper part of the permafrost wedge, creating a subsurface temperature minimum (Fig. 1*B*), in which heat flows from above and below. While the flux of heat from above contributes to the warming within the permafrost wedge, the seafloor temperature, anchored by the −1.4 °C bottom water (16, 17), prevents permafrost from thawing at the top of the permafrost wedge. However, the shift in the subsurface temperature gradient since transgression has warmed the lower part of the permafrost wedge, thawing relic permafrost and producing groundwater (Fig. 1 *B* and *C*) (15, 18, 43). Models of the impact of transgression on subsea permafrost have recognized the potential existence of a slowly moving groundwater system under the relict permafrost wedge that carries waters that are warmer than the permafrost body seaward (18). We envisage that the rough denuded terrain near the shelf edge is the discharge area for the warmed groundwater released by the decay of relict permafrost (Fig. 1 *B* and *C*). The thawing induced by the ascending groundwater results in the thinning and landward retreat of the permafrost wedge. The model prediction of a glacial-age source of freshwater to the outer shelf edge was confirmed by the low chloride concentration and isotopic composition of porewaters sampled along the shelf edge (28). Where groundwater coming from the depth has risen toward the seabed along the seaward edge of the permafrost, its sensible heat has caused thawing of permafrost beneath the denuded zone (Fig. 1 *B* and *C*). The excess ice associated with the relict permafrost has been replaced by water-filled cavities. Estimates of groundwater discharge rates at the shelf edge are between 200 and 350 mm m^{-2} yr^{-1} (18). The temperature of the groundwater discharge is not known, but if it is 1 °C above freezing, the amount of heat carried over the last 12,000 y is enough to melt an ice column up to 40 m thick. The average subsidence of 9 m in the denuded zone could thus be accounted for by thawing in the sediment column of various proportions of segregated and pore ice. The transition from ice to water-filled cavities weakens the sediment column which may lead to either slow bottom settlement or periodic collapses, similar to thaw slumps associated with permafrost degradation observed onshore (4–8). As with karst

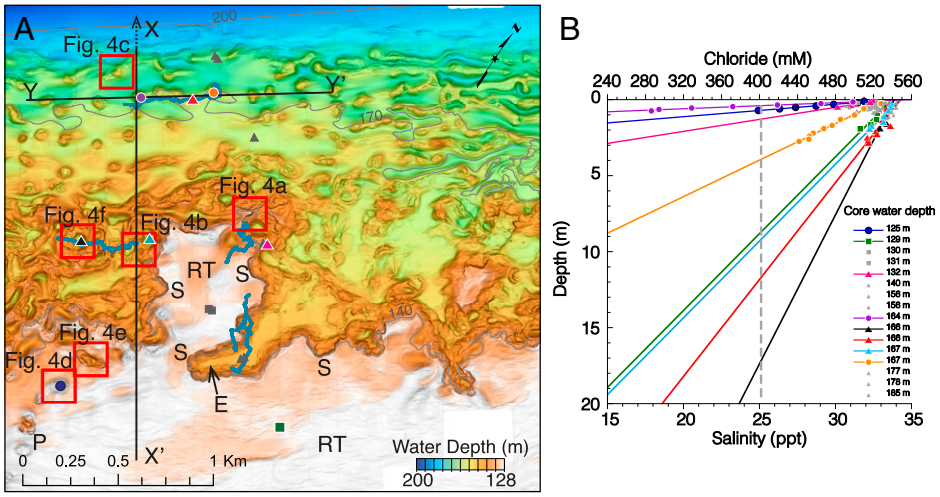

Fig. 5. (*A*) AUV multibeam bathymetry collected during the 2017 AUV survey. Locations of bathymetry shown in Fig. 4 (red squares); cores (colored symbols); ROV dives (blue paths); position of Chirp profiles X-X′ and Y-Y′ shown in Fig. 2*C*; and morphological labels E, RT, and S are indicated. (*B*) Plot of porewater chloride concentrations versus subbottom depth. In the plot legend, colored symbols with lines indicate cores with statistically significant chloride gradients; gray symbols are cores without statistically significant chloride gradients. The dashed gray line is the freezing point for water with 25.3-ppt salinity at −1.5 °C (45). Data from ref. 28.

formation on land, the sea bottom processes may lag substantially behind the rate at which the subsurface volume loss occurs.

Formation of Open System Submarine Pingos. The PLFs within the slope PLF band along with the associated ridges and troughs are embedded within tilted well-layered marine sediments of postglacial age (25–27) (LS, Fig. 2*D*), indicating that they formed during the Holocene. The freshening chloride gradients in cores from this area show that brackish groundwaters are present under the slope PLF band, beyond the maximum limit of glacial-age permafrost (Figs. 1 and 2*C*). These waters are inferred to be part of the same brackish water body that moves under the permafrost. In situ sediment temperature measurements confirm that the upper 3 mbsf in the outer shelf and upper slope are at negative temperatures ranging from −1.2° to −1.4 °C (44). Even at −1.2 °C, waters of 20-ppt salinity (corresponding to ∼319 mM chloride) are at the freezing point (45) (Fig. 5*B*). Thus, conditions near the seafloor are appropriate for the formation of intrasediment ice in excess of the sediment pore space (37, 38). Ground ice including clasts, pore space filling, and thin lenses have been sampled within 2.3 m of the seafloor from the crests of several PLFs (28, 29). As with terrestrial pingos and other ice blisters (46), volume expansion associated with freezing porewaters and formation of segregated ice provides a mechanism to dome the seafloor (19, 46, 47). The PLFs are indeed a submarine version of the onshore pingos (19).

The density of these submarine pingos (19.6 per km^2; based on >550 pingos within the 28 km^2 area mapped in 2019), which is higher than pingo density known elsewhere (20, 48). The numerous pingos along the shelf-slope transition would indicate a sustained supply of brackish groundwater. No changes in pingo morphology were detected, suggesting their rate of growth is beyond the detection limit of elevation change of the repeat mapping surveys. Isotopic measurements made on the brackish porewaters of sediments in the slope PLF belt indicate a source of meteoric waters with a glacial terrestrial signature (28) consistent with decomposed relict permafrost.

The depth mbsf to which freezing occurs is controlled by the thermal gradient. While to date we have not collected any deep cores from a pingo on the slope, a 39 m long core of a PLF on the outer shelf encountered ∼20 to 40% excess ice (32). If the ice content in the slope pingo band is similar, freezing to a depth of ∼25 to 50 m could account for the heave responsible for pingo formation within the slope pingo band. The seafloor thermal gradient will be compressed where the flow of migrating groundwater is higher, presumably reducing the thickness of the surface freezing underneath the denuded zone.

The range of pingo morphologies suggests a geomorphic evolution where sites of focused near seafloor seepage initially form pingos but subsequently evolve into depressions (Fig. 4 *C*–*E*). The development of segregated subsurface ice near the seafloor, where brackish waters ascend until they encounter colder temperatures and freeze, produces initially smooth surfaced pingos. Expansion associated with subsurface ice growth deforms the overlying and surrounding host sediments and generates cracks on the seafloor, especially on the top of pingos, which become conduits through which dense seawater invades the porewater space. The increased salinity of porewaters lowers the melting point of the segregated ice. Ground ice directly exposed to bottom waters of −1.4 °C and salinity of no less than 23.5 ppt (375 mM Cl) will melt (Fig. 5*B*) (45), producing small depressions where pingos were previously. Some depressions on pingos have rims which are apparently vestiges of the upturned flank of former pingos (Fig. 4 *D* and *E*) similar to the collapsed pingos on land (19, 49). While collapsed pingos leave the surrounding sediments deformed, no sediment is lost, and no net change in surface elevation occurs. In contrast, significant net volume loss occurs where relict Pleistocene permafrost ice is melted by ascending groundwater leaving a denuded as well as deformed seafloor morphology.

In summary, we attribute the rough seafloor morphology along the Arctic shelf edge to the flow of groundwater that thaws relict permafrost at depth but freezes in proximity to the seafloor (Fig. 1). Thawing along the edge of the relict permafrost increases permeability and forms enhanced conduits for fluid flow, further adding to the latent heat delivery and accelerating permafrost degradation. Where segregated relict permafrost ice has thawed, the absence of a solid phase to support the overburden leaves the overlying seafloor susceptible to settlement which occurs as periodic collapses. Deformation of near-seafloor sediments also takes

place when ascending groundwaters encounter colder temperatures close to the seafloor and freeze, promoting heaving. However, subsequent infiltration of seawater into the porewater space lowers the melting point of ice inducing thawing with no net loss of volume. It is only where melting of submarine permafrost takes place that substantial subsurface volume losses occur. The observable impact on the seafloor morphology may be greatest at the seaward edge of the relict permafrost wedge where the dwindling relict permafrost wedge is thin and retreating laterally (Fig. 1*C*). The volume loss manifests as a retreat of submarine scarps or collapse depressions, which could serve as telltale signs of relict permafrost thawing elsewhere in the Arctic shelves.

Materials and Methods

Regional multibeam mapping surveys covering the shelf edge and slope in the Canadian Beaufort Sea were conducted from the Canadian Coast Guard ice breaker *Amundsen* in 2010 using a Kongsberg EM302 30-kHz multibeam sonar which provided 4-m grid resolution bathymetry at the relevant water depths (www.omg.unb.ca/Projects/Arctic/). In 2013 and 2017, AUV surveys were launched from the Canadian Coast Guard ice breaker *Sir Wilfrid Laurier* and Korean Polar Institute ice breaker *Araon*, respectively. The AUV was designed for high-resolution seafloor mapping (50) and carried a Reson 7125, 200-kHz multibeam sonar in 2013; a Reson 7125, 400-kHz in 2017; and an Edgetech 1- to 6-kHz chirp subbottom profiler on both surveys. The AUV was programmed to proceed to preset waypoints which provided ∼150-m-spaced track lines while maintaining an altitude of 50 m off the seafloor. In this mode, overlapping multibeam bathymetric coverage was obtained which is independent of water depth and provides a vertical resolution of 0.15 m and a horizontal footprint of 0.87 m. During each AUV dive, up to 9 km^2 of the seafloor was surveyed. Initial navigation fixes were obtained from the global positioning system (GPS) when on the surface and subsequently updated with a Doppler velocity log and a Kearfott inertial navigation system. Chirp seismic-reflection profiles provide 30-cm vertical resolution imaging of the shallow sediment stratigraphy. The 2019 surveys were conducted from the Canadian Coast Guard icebreaker *Sir Wilfrid Laurier*, using a Konsberg EM2040C 200- to 400-kHz multibeam system, which provided 2-m grid resolution bathymetry. The multibeam data from all four surveys were processed using the open source software package MB-System (51). MBNavadjust (www3.mbari.org/products/mbsystem/html/mbnavadjust.html) was used to colocate the AUV surveys in relation to the GPS-navigated 2010 and 2019 surveys. To provide difference maps, the surveys were subtracted at 4-m grid resolution. The 2013 and 2017 AUV multibeam data, as well as the 2019 surface ship multibeam survey, are available at https://www.marine-geo.org/tools/search/entry.php?id=Arctic_MBARI, with DOIs 10.26022/IEDA/330272, 10.26022/IEDA/330278, and 10.26022/IEDA/330278, respectively. Additional data are available at https://www.mbari.org/arctic-shelf-edge. Five ROV dives conducted in the areas of overlapping surveys provided video observations of the seafloor and water column temperatures. Porewater chloride data on 17 sediment cores collected from within the AUV-surveyed areas are published (28).

Data Availability. Multibeam bathymetry data have been deposited in Marine Geoscience Data System (https://www.marine-geo.org/tools/search/entry.php?id=Arctic_MBARI) (52).

ACKNOWLEDGMENTS. Support was provided by David and Lucile Packard Foundation, Geological Survey of Canada, Fisheries, and Oceans Canada and the Korean Ministry of Ocean and Fisheries (KIMST Grant 1525011795).

Author affiliations: [a]Science Division, Monterey Bay Aquarium Research Institute, Moss Landing, CA 93039; [b]Geological Survey of Canada, Natural Resources Canada, Sidney, BC V8L 4B2, Canada; [c]Department of Earth Sciences, Korean Polar Research Institute, Incheon 21990, Korea; [d]Center for Coastal & Ocean Mapping/Joint Hydrographic Center, University of New Hampshire, Durham, NH 03824; [e]Canadian Hydrographic Service, Fisheries and Oceans Canada, Burlington, ON F7S 1A1, Canada; and [f]Institute of Ocean Sciences, Fisheries and Oceans Canada, Sidney, BC V8L 4B2, Canada

1. S. E. Chadburn *et al.*, An observation-based constraint on permafrost loss as a function of global warming. *Nat. Clim. Chang.* **7**, 340–344 (2017).
2. D. Olefeldt *et al.*, Circumpolar distribution and carbon storage of thermokarst landscapes. *Nat. Commun.* **7**, 13043 (2016).
3. T. Osterkamp, M. Jorgenson, Response of boreal ecosystems to varying modes of permafrost degradation in Alaska. *Can. J. For. Res.* **35**, 2100–2111 (2005).
4. A. G. Lewkowicz, R. G. Way, Extremes of summer climate trigger thousands of thermokarst landslides in a High Arctic environment. *Nat. Commun.* **10**, 1329 (2019).
5. L. Armstrong, D. Lacelle, R. H. Fraser, S. Kokelj, A. Knudby, Thaw slump activity measured using stationary cameras in time-lapse and structure-from-motion photogrammetry. *Arct. Sci.* **4**, 827–845 (2018).
6. K. R. Barnhart *et al.*, Modeling erosion of ice-rich permafrost bluffs along the Alaskan Beaufort Sea coast. *J. Geophys. Res. Earth Surf.* **119**, 1155–1179 (2014).
7. R. Fraser *et al.*, Climate sensitivity of High Arctic permafrost terrain demonstrated by widespread ice-wedge thermokarst on Banks Island. *Remote Sens.* **10**, 954 (2018).
8. H. Lantuit *et al.*, Modern and late Holocene retrogressive thaw slump activity on the Yukon Coastal Plain and Herschel Island, Yukon Territory, Canada: Modern and late Holocene slump activity on the Yukon Coast. *Permafr. Periglac. Process.* **23**, 39–51 (2012).
9. J. R. Mackay, Offshore permafrost and ground ice, Southern Beaufort Sea, Canada. *Can. J. Earth Sci.* **9**, 1550–1561 (1972).
10. B. R. Pelletier, *Marine Science Atlas of the Beaufort Sea: Geology and Geophysics* (Geological Survey of Canada, 1987), 10.4095/126940.
11. K. Lambeck, H. Rouby, A. Purcell, Y. Sun, M. Sambridge, Sea level and global ice volumes from the Last Glacial Maximum to the Holocene. *Proc. Natl. Acad. Sci. U.S.A.* **111**, 15296–15303 (2014).
12. A. E. Taylor, Marine transgression, shoreline emergence: Evidence in seabed and terrestrial ground temperatures of changing relative sea levels, Arctic Canada. *J. Geophys. Res. Solid Earth* **96**, 6893–6909 (1991).
13. P. P. Overduin *et al.*, Submarine permafrost map in the Arctic modeled using 1-D transient heat flux (SuPerMAP). *J. Geophys. Res. Oceans* **124**, 3490–3507 (2019).
14. S. Pullan *et al.*, "Permafrost distribution determined from seismic refraction" in *Marine Science Atlas of the Beaufort Sea: Geology and Geophysics*, B. R. Pelletier, Ed. (Geological Survey of Canada, 1987), pp. 37.
15. A. E. Taylor *et al.*, Numerical model of the geothermal regime on the Beaufort Shelf, arctic Canada since the Last Interglacial: numerical model, Beaufort Sea Permafrost. *J. Geophys. Res. Earth Surf.* **118**, 2365–2379 (2013).
16. F. A. McLaughlin *et al.*, The joint roles of Pacific and Atlantic-origin waters in the Canada Basin, 1997–1998. *Deep Sea Res. Part Oceanogr. Res. Pap.* **51**, 107–128 (2004).
17. H. Melling, Hydrographic changes in the Canada Basin of the Arctic Ocean, 1979-1996. *J. Geophys. Res. Oceans* **103**, 7637–7645 (1998).
18. J. M. Frederick, B. A. Buffett, Effects of submarine groundwater discharge on the present-day extent of relict submarine permafrost and gas hydrate stability on the Beaufort Sea continental shelf. *J. Geophys. Res. Earth Surf.* **120**, 417–432 (2015).
19. J. R. Mackay, Pingo growth and collapse, Tuktoyaktuk Peninsula Area, Western Arctic Coast, Canada: A long-term field study. *Géogr. Phys. Quat.* **52**, 271–323 (2002).
20. G. Grosse, B. M. Jones, Spatial distribution of pingos in northern Asia. *Cryosphere* **5**, 13–33 (2011).
21. J. M. Shearer, R. F. Macnab, B. R. Pelletier, T. B. Smith, Submarine pingos in the Beaufort Sea. *Science* **174**, 816–818 (1971).
22. C. K. Paull *et al.*, Origin of pingo-like features on the Beaufort Sea shelf and their possible relationship to decomposing methane gas hydrates. *Geophys. Res. Lett.* **34**, L01603 (2007).
23. J. F. Nixon, N. R. Morgenstern, Thaw–consolidation tests on undisturbed fine-grained permafrost. *Can. Geotech. J.* **11**, 202–214 (1974).
24. E. Chuvilin *et al.*, Conceptual models of gas accumulation in the shallow permafrost of Northern West Siberia and conditions for explosive gas emissions. *Geosciences (Basel)* **10**, 195 (2020).
25. F. Saint-Ange *et al.*, Multiple failure styles related to shallow gas and fluid venting, upper slope Canadian Beaufort Sea, Northern Canada. *Mar. Geol.* **355**, 136–149 (2014).
26. L. D. Keigwin *et al.*, Deglacial floods in the Beaufort Sea preceded Younger Dryas cooling. *Nat. Geosci.* **11**, 599–604 (2018).
27. C. K. Paull *et al.*, A 100-km wide slump along the upper slope of the Canadian Arctic was likely preconditioned for failure by brackish pore water flushing. *Mar. Geol.* **435**, 106453 (2021).
28. R. Gwiazda *et al.*, Freshwater seepage into sediments of the shelf, shelf edge, and continental slope of the Canadian Beaufort Sea. *Geochem. Geophys. Geosyst.* **19**, 3039–3055 (2018).
29. Y. K. Jin, S. R. Dallimore, "ARA05C Marine Research Expedition Canada-Korea-USA Beaufort Sea Geoscience Research Program: Summary of 2014 activities" (Geological Survey of Canada, Open File 7999, 2016).
30. V. Bogoyavlensky *et al.*, New catastrophic gas blowout and giant crater on the Yamal Peninsula in 2020: Results of the expedition and data processing. *Geosciences (Basel)* **11**, 71 (2021).
31. T. S. Collett, A. Johnson, C. C. Knapp, R. Boswell, *Natural Gas Hydrates: Energy Resource Potential and Associated Geologic Hazards*, AAPG Memoir (AAPG, 2010, vol. **89**).
32. E. Banke, Report on coring program of a pingo-like sub-sea mound at Admirals Finger, Beaufort Sea, summer 1979. *Arct. Sci. Technol. Inf. Syst.* (1980).
33. A. S. Dyke, W. R. Peltier, Forms, response times and variability of relative sea-level curves, glaciated North America. *Geomorphology* **32**, 315–333 (2000).
34. A. S. Dyke, "An outline of North American deglaciation with emphasis on central and northern Canada" in *Developments in Quaternary Sciences*, J. Ehlers, P. L. Gibbard, Eds. (Elsevier, 2004), pp. 373–424.
35. J. H. England, M. F. A. Furze, J. P. Doupé, Revision of the NW Laurentide Ice Sheet: Implications for paleoclimate, the northeast extremity of Beringia, and Arctic Ocean sedimentation. *Quat. Sci. Rev.* **28**, 1573–1596 (2009).
36. K. Hu, D. R. Issler, Z. Chen, T. A. Brent, *Permafrost Investigation by Well Logs, and Seismic Velocity and Repeated Shallow Temperature Surveys* (Beaufort-Mackenzie Basin, 2013).
37. J. R. Mackay, The origin of massive icy beds in permafrost, Western Arctic Coast, Canada. *Can. J. Earth Sci.* **8**, 397–422 (1971).
38. J. R. Mackay, S. R. Dallimore, Massive ice of the Tuktoyaktuk area, western Arctic coast, Canada. *Can. J. Earth Sci.* **29**, 1235–1249 (1992).

39. M. Riedel, J. K. Hong, Y. K. Jin, H. S. Kim, "Refraction seismic velocity analyses from multichannel seismic data acquired during Expedition ARA04C on the IBRV Araon in the Beaufort Sea" (Geological Survey of Canada, Open File 7618, 2014).
40. M. Z. Li, E. L. King, D. Schillinger, A. G. Robertson, Y. Wu, "Observation of bottom currents and sediment transport from the 2015-2016 year-long deployment of a seabed lander on the shelf edge of the Beaufort Sea, offshore Northwest Territories" (Geological Survey of Canada, Open File 8553, 2019).
41. W. Dobiński, Permafrost active layer. *Earth Sci. Rev.* **208**, 103301 (2020).
42. B. J. Phrampus, M. J. Hornbach, C. D. Ruppel, P. E. Hart, Widespread gas hydrate instability on the upper U.S. Beaufort margin: U.S. Beaufort Margin Hydrate Instability. *J. Geophys. Res. Solid Earth* **119**, 8594–8609 (2014).
43. M. Riedel *et al.*, Evidence for gas hydrate occurrences in the Canadian Arctic Beaufort Sea within permafrost-associated shelf and deep-water marine environments. *Mar. Pet. Geol.* **81**, 66–78 (2017).
44. M. Riedel, H. Villinger, K. Asshoff, N. Kaul, S. R. Dallimore, "*Temperature measurements and thermal gradient estimates on the slope and shelf-edge region of the Beaufort Sea Canada*" (Geological Survey of Canada, Open File 7725, 2015).
45. F. J. Millero, W. H. Leung, The thermodynamics of seawater at one atmosphere. *Am. J. Sci.* **276**, 1035–1077 (1976).
46. S. A. Wolfe, C. W. Stevens, A. J. Gaanderse, G. A. Oldenborger, Lithalsa distribution, morphology and landscape associations in the Great Slave Lowland, Northwest Territories, Canada. *Geomorphology* **204**, 302–313 (2014).
47. J. B. Murton, R. Peterson, J.-C. Ozouf, Bedrock fracture by ice segregation in cold regions. *Science* **314**, 1127–1129 (2006).
48. B. M. Jones *et al.*, Assessment of pingo distribution and morphometry using an IfSAR derived digital surface model, western Arctic Coastal Plain, Northern Alaska. *Geomorphology* **138**, 1–14 (2012).
49. J. R. Mackay, C. R. Burn, A century (1910-2008) of change in a collapsing pingo, Parry Peninsula, Western Arctic Coast, Canada: Pingo collapse, Parry Peninsula. *Periglac.Process.* **22**, 266–272 (2011).
50. D. Caress *et al.*, "High-resolution multibeam, sidescan, and subbottom surveys using the MBARI AUV D. Allan B" in *Marine Habitat Mapping Technology for Alaska*, J. Reynolds, H. Greene, Eds. (Alaska Sea Grant, University of Alaska Fairbanks, 2008), pp. 47–70.
51. D. W. Caress, D. N. Chayes, Improved processing of Hydrosweep DS multibeam data on the R/V Maurice Ewing. *Mar. Geophys. Res.* **18**, 631–650 (1996).
52. C. K. Paull, Near-bottom surveys of the continental slope of the Canadian Beaufort Sea. MGDS. https://www.marine-geo.org/tools/search/entry.php?id=Arctic_MBARI. Deposited 16 November 2021.